Title: Human Emissions Drive the Pacific Decadal Oscillation

Authors: Jeremy M. Klavans[1*], Pedro N. DiNezio[1], Amy C. Clement[2], Clara Deser[3], Timothy M. Shanahan[4]

Affiliations:

[1]Department of Atmospheric and Oceanic Sciences, University of Colorado Boulder; Boulder, CO, USA.

[2]Rosenstiel School of Marine, Atmospheric, and Earth Science, University of Miami; Miami, FL, USA.

[3]National Center for Atmospheric Research; Boulder, CO, USA.

[4]Jackson School of Geosciences, University of Texas at Austin; Austin, TX, USA.

*Corresponding author. Email: jeremy.klavans@colorado.edu

Abstract: The Pacific Decadal Oscillation (PDO) – a major mode of climate variability driving changes over the North Pacific Ocean and surrounding continents – is currently thought to be generated by naturally-occurring processes in the climate system. Using an exceptionally large ensemble of climate model simulations, we show that recent shifts in the PDO index were driven by human emissions of aerosols and greenhouse gases. This anthropogenic influence had previously gone undetected because models underestimate air-sea interactions amplifying temperature variations in the North Pacific. By rescaling the simulations to mitigate this issue, we demonstrate that observed PDO impacts – including the current drought in the western United States – can be largely attributed to human activity via externally forced changes in the PDO.

One-Sentence Summary: Climatic variations in the North Pacific and on surrounding continents are now attributable to human activity.

Main Text:

The Pacific Decadal Oscillation (PDO) – the leading pattern of North Pacific sea-surface temperature (SST) variability (*1, 2*) – is associated with persistent changes in global and regional climate, including the rate of global warming (*3*), the ongoing drought in the western United States (U.S.; *4*), and the accelerated rates of sea level rise affecting vulnerable island states in the western Pacific (*5*). This SST pattern fluctuates between its warm- and cold-states on multidecadal timescales (*6*). The timing of these shifts is thought to be governed by natural processes in the climate system, including random atmospheric circulation variability, local ocean dynamics, and coupled tropical variability (*6 - 8*). By simulating these processes, dynamical and statistical models can produce a PDO that has a realistic spatial pattern (*5*). However, these models underestimate the strength of the PDO on multidecadal timescales (*9*). Perhaps because of this missing low-frequency variability, models cannot predict the PDO and its impacts on society far in advance (*10, 11*). This missing variability reflects a gap in our understanding of the slow, potentially predictable, components of the PDO.

Conventional models of the PDO do not consider external radiative forcing despite its outsized influence on recent long-term climate changes, such as the observed global warming trend, as well as regional patterns of multidecadal climate variability (*8*). For example, large changes in the emissions of aerosols and greenhouse gases explain recent multidecadal variations in North Atlantic and European climate (*12 – 15*). In contrast, no such influence has yet been identified in the North Pacific (*6, 8, 16, 17*), despite large changes in external forcing over the last several decades (*18, 19*). Studies indicating a possible role for external forcing in North Pacific climate variability have been limited to either a single climate model (20 - 23) or restricted to the most recent decades (*24 - 26*), thus failing to robustly establish an anthropogenic influence on the PDO.

Here we study anthropogenic influences on North Pacific climate variability using an exceptionally large ensemble of climate model simulations. We construct the ensemble with 572 simulations from 12 different climate models across two generations of model development and use this ensemble to isolate the forced variations in the PDO. This multimodel approach ensures that results are applicable beyond the idiosyncrasies of a single model or the complexity of representation of physical processes, particularly those involving aerosols (Table S1). Each simulation in this ensemble is forced by a combination of all the major sources of changes in external forcing, including greenhouse gas and aerosol emissions, volcanic eruptions, and solar variability. We isolate individual sources of external forcing using 286 additional simulations, each of which includes changes in only a single forcing agent separately: greenhouse gases, industrial aerosols, or natural sources (volcanic eruptions and solar cycles). A minimum of 75 of these "single-forcing" simulations were performed for each forcing agent using 5 distinct climate models (Table S2). If the forced response in a particular ensemble of single-forcing simulations can reproduce the timing and pattern of the observed PDO, we attribute PDO changes to that forcing agent. The bulk of our analysis focuses on the 1950-2014 period common to all 827 simulations, although we consider the full length of simulations dating back to 1850 when possible. We characterize climate variability in the North Pacific using the traditional PDO index, defined as the first principal component of North Pacific annual average SST after removing the global warming signal (*2*). Alternative definitions of the PDO index (see Methods) yield similar results to those presented below, ensuring that our conclusions are not an artifact of a known relationship between Pacific climate variability and global mean temperatures (Fig. S1; *27*). To focus on multidecadal variability, we remove interannual variability associated with the El Niño – Southern Oscillation. In observations, we remove these interannual fluctuations via linear regression. In models, ensemble averaging removes interannual variability because the occurrence of El Nino and La Nina events is uncorrelated amongst model runs. We then low-pass filter both the observed and simulated PDO indices to isolate variability with periods longer than 10 years (see Methods).

We find that changes in external forcing explain key multidecadal shifts in the observed PDO index after 1950. Between 1950 and 2014, the externally forced PDO explains 53% of observed multidecadal PDO index variance (r^2) and successfully reproduces key PDO transitions in the 1970s and 1990s (Fig. 1a). This correlation is statistically significant at the 95% threshold, accounting for the fewer available degrees of freedom after low-pass filtering (see Methods). The robustness of this result is supported by further metrics allowed by the novel size and breadth of this ensemble. First, the forced PDO index explains more variance in the observed PDO index than 98% of the individual model runs (Fig. S2a). That is, in models, there is only a two percent chance that natural variability alone is a better explanation of the multidecadal shifts in the PDO than external forcing. Second, this correlation is found for nearly all models included in the ensemble (Fig. S3) confirming it is not a random result arising from the reduced degrees of freedom in the timeseries. Third, the forced PDO index matches the observed inflection point in the mid-1990s from a positive to a negative trend within a few years, whereas natural variability in climate models generates changes in the PDO index trend at random (Fig. S2b; Methods). Last, we find that as changes in external forcing grow larger throughout the 20th century, external forcing explains larger shares of PDO variance (Fig. S3). Together these results support our finding that after 1950, external forcing explains most of the timing of multidecadal shifts in the PDO.

The anthropogenic influence on the PDO is robust across models despite their diverse representations of physical processes. Most of the single-model ensembles explain at least a quarter of observed PDO variance after 1950, indicating that our results are not a quirk of the design of an individual model (Fig. S3). That is, models produce similar results despite fundamental differences in the way aerosols are emitted and distributed by their atmospheric components. More thorough inter-model comparisons are difficult given that only two single-model ensembles have the 100 simulations we find are required to isolate the forced PDO (Fig. S4). However, we can group models by their common attributes and create large enough ensembles to isolate the impact of these features on the forced PDO. We find that the contribution of forcing to the PDO is reasonably robust to (1) model generation, (2) the implementation of aerosol emissions, and (3) the complexity of cloud-aerosol interactions (Fig. S4; Table S4). Together these sensitivity analyses show that the substantial role for external forcing in the timing of the PDO index is not an artifact of a single model, numerical approach, or physical process, such as the implementation of aerosol indirect effects.

In addition to explaining key observed shifts in the PDO, the forced PDO index is associated with an SST pattern in models that bears striking resemblance to the observed PDO pattern. During its positive phase, the observed and simulated SST patterns show similar cooler than normal ocean temperatures over the western and central North Pacific, surrounded by a horseshoe of warmer than normal surface waters along the North American coast (Fig. 1b and 1c). CMIP5 models are particularly skillful at reproducing this forced pattern (Fig. 1c), generating a more realistic externally forced SST pattern than CMIP6 models (Fig. S5f). Like in the real world, the positive phase of the forced PDO in models is associated with a deepening of the Aleutian Low, the semi-permanent low-pressure system over the North Pacific during boreal winter (Fig. 1c, contours). The forced PDO pattern is robust across individual model ensembles and to their representation of complex physical processes (Fig. S5 and S6). The realism of the forced SST pattern in models serves as further evidence that external forcing is a physical contributor to the real world PDO.

Models show that the observed multidecadal shifts in the PDO index arise from the interplay between industrial aerosols and greenhouse gasses. Between 1950 and the mid-1980s, rapidly rising emission and concentrations of industrial aerosols (*18*) coincide with the long positive trend in the PDO index that characterized this period (Fig. 1a). When forced with only industrial aerosols, models faithfully reproduce this positive trend (Fig. 2a and 2d). In the late-1980s, this positive trend reverses, as aerosol emissions declined (*18*) and greenhouse gas warming became the dominant climate forcing (IPCC 2021; Fig 1a, 2a, and 2b). Models forced with only industrial aerosols produce a flattening of the positive trend after the mid-1980s following the decline in aerosol emissions (Fig. 2a). The observed downward trend in the PDO after 1990 is better explained when models are forced with only greenhouse gases, which drive a negative trend in the PDO (Fig. 2b and 2d). Therefore, declining industrial aerosol concentrations together with rising greenhouse gas concentrations drove the mid-1980s inflection in the PDO index. In contrast, natural forcings, i.e. from solar cycles and volcanic eruptions, only explain a small part of the temporal evolution of the PDO (1% of the variance, Fig. 2c and 2d).

While we have shown that aerosol and greenhouse gas emissions drive multidecadal variations in the PDO, the amplitude of the simulated response is much weaker than in observations (Fig. 1a; Table S3). As a result, the much larger, naturally generated climate variability or "noise" produced by models overwhelms the forced PDO signal in each individual simulation of historical climate. Similarly, models underestimate forced variability relative to naturally generated variability in the North Atlantic (*14, 28*). The resulting low signal-to-noise ratio produces the puzzling result that a model's forced response can better predict observed variability than it can predict the variability in an individual simulation performed with that model (*29, 30*). Our results reflect a similar "signal-to-noise paradox" (*30*), but for North Pacific SSTs, demonstrating that this error broadly affects low-frequency climate variability throughout the Northern Hemisphere, and potentially throughout the globe.

We infer the mechanisms by which external forcing excites the PDO by comparing the spatial pattern of the forced response in models to the large-scale patterns of variability in observations. Forced SST variations in the western North Pacific have the largest amplitude relative to observations, particularly along the front in the Kuroshio-Oshashio Extension (KOE) region off the coast of Japan (Fig. 3a). In this region, external forcing explains roughly half of the observed SST variability amplitude (Fig. 3a) indicating that the signal-to-noise error is less severe there. The SST response over the KOE is likely driven by some combination of (1) advection of cooler or warmer continental air generated over Eurasia by aerosols or greenhouse warming (*31*), (2) changing land-sea temperature contrast producing relative cooler or warmer air that is also advected over the KOE region, or (3) the advection of pollution from aerosol emitting regions in Asia. Because the forced response is much larger in this region than the rest of the North Pacific, we hypothesize that aerosols and greenhouse gases influence the PDO by affecting SSTs in the KOE, but a missing mechanism in models fails to convey the forced response to the rest of the North Pacific.

The mechanisms communicating the forced response to the rest of the North Pacific likely involve changes in the strength of the Aleutian Low – the semipermanent low-pressure system controlling surface winds over the North Pacific. In models, the forced PDO index is highly correlated with the forced variations in the strength of the Aleutian Low ($r^2 = 0.7$; Fig. 3b; see Methods), consistent with a well-established simultaneous relationship between these processes in observations. This high correlation can be created by multiple coupled processes. In climate models without anthropogenic forcing, high correlations predominately emerge when stochastic variations in the Aleutian Low drive contemporaneous changes in the PDO SST pattern (*6*). In recent observations and, potentially in the forced response identified here, high correlations could also be indicative of changes in the strength of the Aleutian Low driven by SST variations in the KOE region (*32 - 34*). This response also involves an amplifying feedback whereby thermal advection by wind-driven ocean currents reinforces SST variability over the KOE region (*35*). The strength of this positive, coupled ocean-atmosphere feedback will depend on the magnitude of the Aleutian Low response to KOE SSTs, which we quantify by regressing forced sea-level pressure variations on forced SST variations in the KOE region (Fig. 3c and 3d). We find that in models the strength of this feedback is much weaker (~1 hPa/degC; Fig. 3c) than in observations (5 hPa/degC; Fig. 3d), indicating that forced SST variations in the KOE fail to excite the Aleutian Low in models with the same vigor as the real world. The tepid variations in the Aleutian Low then fail to convey the full forced signal to the rest of the basin, resulting in a much weaker ratio of forced-to-observed variability in the eastern North Pacific (~0.1) relative to the ratio over the KOE (~0.5; Fig. 3a).

One possible explanation for this muted Aleutian Low response in models could be related to a misrepresentation of atmospheric processes in climate models. A previous study showed that atmospheric models run at the conventional resolution of 1 degree fail to excite a realistically strong atmospheric response to SST changes over the North Pacific (*36*). This study also suggests that models would need to be run at a resolution of greater than ¼ degree to induce a realistic atmospheric response to KOE SSTs, which currently incurs prohibitive computational costs. This issue might be exacerbated by other model deficiencies related to their ability to resolve small scale processes in the ocean. For example, positive ocean feedbacks in the western North Pacific (*35*) tend to be underestimated in climate models without fully resolved western boundary current SST fronts (*37*) and can result in a weaker atmospheric response to externally forced SST variability. Further, models may also underestimate the direct influence of aerosol forcing on the Aleutian Low (*38*), but this would not explain the greenhouse forced period nor the spatial pattern of forced variability (Fig 3a).

The failure of climate models to simulate the full amplitude of the forced PDO has clouded our view of the recent history of global climate. In the early 2000s, a "hiatus" in global warming was largely attributed to a naturally generated PDO-like pattern of cooling in the Pacific Ocean (*3, 39*). However, we have shown that this pattern is a response to external forcing that is underestimated in climate models. We expect that mitigating signal-to-noise errors in climate models will amplify the forced PDO and therefore better explain global mean temperatures at the beginning of the 21st century. Further, by mitigating this error in models we may also rectify known biases in the simulation of externally forced trend in the tropical Pacific (*40*). Climate models simulate a forced El Niño-like trend in the tropical Pacific over the last few decades (*41*), which is at odds with the flat or La Niña-like trend in observations and theory (*42, 43*). A stronger tropical component of the forced PDO in models may help correct the east-west SST gradient by driving a cooling trend in the eastern tropical Pacific after about 1990, through for example the wind-evaporation-SST feedback (*44, 45*).

The idea that the ongoing meteorological drought in the western US is driven by natural, albeit unlucky combination of variations in the climate system, associated with the PDO (*46, 47*) also needs to be reevaluated in light of our findings that models may underestimate the forced response of the PDO. Western US drought was previously thought to be natural because: (1) the magnitude of the observed precipitation decline between 1982-2012 (16.5%) was much larger than could be generated by known external forcings (3.4%) and (2) drying trends as dramatic as observations only occur in 20% of simulations (Fig. 4b). However, we have shown that the PDO has a large, externally forced component that is underestimated by climate models. Artificially rescaling the forced PDO in models to be 53% of the total PDO (our estimate of the forced contribution to the observed PDO) produces precipitation deficits that are in good agreement with observations (-14.7%), and more commonplace, occurring in about half of the individual simulations (49%; Fig. 4b). This provides additional support for an anthropogenic driver of observed PDO variability and ongoing meteorological drought – due to a combination of aerosol and greenhouse gases.

Overall, we find that human activity is a key contributor to the PDO over the last seven decades. Aerosol emissions drove the positive trend in the PDO from the 1950s to 1980s. The abatement of industrial aerosols paired with exponentially rising greenhouse gas emissions are driving the ongoing negative trend in the PDO. This history of external forcing will thus explain PDO impacts over the past seven decades, including the ongoing drought in the western U.S. as shown here, as well as, for example, sea level trends over the North Pacific. The role of forcing in the PDO was previously obscured by an unrealistically low signal-to-noise ratio in climate models, which we mitigate with an extraordinarily large ensemble of climate model simulations. We find that the small amplitude of the forced PDO is related to an under-simulated Aleutian Low response to external forcing. Resolving signal-to-noise errors in climate models will allow for more accurate predictions of global and regional climate by accounting for the expanded role of external forcing we identify here. Promising recent work shows that increasing model resolution may help mitigate the signal-to-noise paradox (*48, 49*) by improving the simulation of both oceanic (*37, 50*) and atmosphere-ocean feedbacks (*36*). As new solutions to improve climate models are implemented, large ensembles of current generation models still hold the power to reveal additional, critical risks of continued long term global warming over the United States. We expect that the drought in the western U.S. will continue, as it is unlikely that random atmospheric variability or an altered state of the PDO will bring more rainfall over the next decades.

References and Notes

1. Mantua, N. J., Hare, S. R., Zhang, Y., Wallace, J. M., & Francis, R. C., A Pacific Interdecadal Climate Oscillation with Impacts on Salmon Production. *Bulletin of the American Meteorological Society*, *78*(6), (1997). 1069–1080.
2. Zhang, Y., Wallace, J. M., & Battisti, D. S., ENSO-like Interdecadal Variability: 1900–93. *Journal of Climate*, *10*(5), (1997). 1004–1020.
3. Trenberth, K. E., & Fasullo, J. T., An apparent hiatus in global warming? *Earth's Future*, *1*(1), (2013). 19–32.
4. McCabe, G. J., Palecki, M. A., & Betancourt, J. L., Pacific and Atlantic Ocean influences on multidecadal drought frequency in the United States. *Proceedings of the National Academy of Sciences*, *101*(12), (2004). 4136–4141.
5. Fasullo, J. T., Gent, P. R., & Nerem, R. S., Forced Patterns of Sea Level Rise in the Community Earth System Model Large Ensemble From 1920 to 2100. *Journal of Geophysical Research: Oceans*, *125*(6), (2020). e2019JC016030.
6. Newman, M., Alexander, M. A., Ault, T. R., Cobb, K. M., Deser, C., Lorenzo, E. D., Mantua, N. J., Miller, A. J., Minobe, S., Nakamura, H., Schneider, N., Vimont, D. J., Phillips, A. S., Scott, J. D., & Smith, C. A., The Pacific Decadal Oscillation, Revisited. *Journal of Climate*, *29*(12), (2016). 4399–4427.
7. Latif, M., & Barnett, T. P., Causes of Decadal Climate Variability over the North Pacific and North America. *Science*, *266*(5185), (1994). 634–637.

8. Eyring, V., N.P. Gillett, K.M. Achuta Rao, R. Barimalala, M. Barreiro Parrillo, N. Bellouin, C. Cassou, P.J. Durack, Y. Kosaka, S. McGregor, S. Min, O. Morgenstern, and Y. Sun, Human Influence on the Climate System. In Climate Change 2021: The Physical Science Basis. Contribution of Working Group I to the Sixth Assessment Report of the Intergovernmental Panel on Climate Change [Masson-Delmotte, V., P. Zhai, A. Pirani, S.L. Connors, C. Péan, S. Berger, N. Caud, Y. Chen, L. Goldfarb, M.I. Gomis, M. Huang, K. Leitzell, E. Lonnoy, J.B.R. Matthews, T.K. Maycock, T. Waterfield, O. Yelekçi, R. Yu, and B. Zhou (eds.)]. Cambridge University Press, Cambridge, United Kingdom and New York, NY, USA, (2021). 423–552.
9. Mann, M. E., Steinman, B. A., & Miller, S. K., Absence of internal multidecadal and interdecadal oscillations in climate model simulations. *Nature Communications*, *11*(1), (2020). 1–9.
10. Newman, M., An Empirical Benchmark for Decadal Forecasts of Global Surface Temperature Anomalies. *Journal of Climate*, *26*(14), (2013). 5260–5269.
11. Boer, G. J., & Sospedra-Alfonso, R., Assessing the skill of the Pacific Decadal Oscillation (PDO) in a decadal prediction experiment. *Climate Dynamics*, *53*(9), (2019). 5763–5775.
12. Borchert, L. F., Koul, V., Menary, M. B., Befort, D. J., Swingedouw, D., Sgubin, G., & Mignot, J., Skillful decadal prediction of unforced southern European summer temperature variations. *Environmental Research Letters*, *16*(10), (2021). 104017.
13. Booth, B. B. B., Dunstone, N. J., Halloran, P. R., Andrews, T., & Bellouin, N., Aerosols implicated as a prime driver of twentieth-century North Atlantic climate variability. *Nature*, *484*(7393), (2012). 228.
14. Klavans, J. M., Cane, M. A., Clement, A. C., & Murphy, L. N., NAO predictability from external forcing in the late 20th century. *Npj Climate and Atmospheric Science*, *4*(1), (2021). 1–8.
15. Menary, M. B., Robson, J., Allan, R. P., Booth, B. B. B., Cassou, C., Gastineau, G., Gregory, J., Hodson, D., Jones, C., Mignot, J., Ringer, M., Sutton, R., Wilcox, L., & Zhang, R., Aerosol-Forced AMOC Changes in CMIP6 Historical Simulations. *Geophysical Research Letters*, *47*(14), (2020). e2020GL088166.
16. Dong, L., Zhou, T., & Chen, X., Changes of Pacific decadal variability in the twentieth century driven by internal variability, greenhouse gases, and aerosols. *Geophysical Research Letters*, *41*(23), (2014). 8570–8577.
17. Hua, W., Dai, A., & Qin, M., Contributions of Internal Variability and External Forcing to the Recent Pacific Decadal Variations. *Geophysical Research Letters*, *45*(14), (2018). 7084–7092.
18. Deser, C., Phillips, A. S., Simpson, I. R., Rosenbloom, N., Coleman, D., Lehner, F., Pendergrass, A. G., DiNezio, P., & Stevenson, S., Isolating the Evolving Contributions of Anthropogenic Aerosols and Greenhouse Gases: A New CESM1 Large Ensemble Community Resource. *Journal of Climate*, *33*(18), (2020). 7835–7858.

19. Hoesly, R. M., Smith, S. J., Feng, L., Klimont, Z., Janssens-Maenhout, G., Pitkanen, T., Seibert, J. J., Vu, L., Andres, R. J., Bolt, R. M., Bond, T. C., Dawidowski, L., Kholod, N., Kurokawa, J., Li, M., Liu, L., Lu, Z., Moura, M. C. P., O'Rourke, P. R., & Zhang, Q., Historical (1750–2014) anthropogenic emissions of reactive gases and aerosols from the Community Emissions Data System (CEDS). *Geoscientific Model Development*, *11*(1), (2018). 369–408.
20. Wang, T., Otterå, O. H., Gao, Y., & Wang, H., The response of the North Pacific Decadal Variability to strong tropical volcanic eruptions. *Climate Dynamics*, *39*, (2012). 2917–2936.
21. Yeh, S.-W., Kim, W.-M., Kim, Y. H., Moon, B.-K., Park, R. J., & Song, C.-K., Changes in the variability of the North Pacific sea surface temperature caused by direct sulfate aerosol forcing in China in a coupled general circulation model. *Journal of Geophysical Research: Atmospheres*, *118*(3), (2013). 1261–1270.
22. Boo, K.-O., Booth, B. B. B., Byun, Y.-H., Lee, J., Cho, C., Shim, S., & Kim, K.-T., Influence of aerosols in multidecadal SST variability simulations over the North Pacific. *Journal of Geophysical Research: Atmospheres*, *120*(2), (2015). 517–531.
23. Diao, C., Xu, Y., & Xie, S.-P., Anthropogenic aerosol effects on tropospheric circulation and sea surface temperature (1980-2020): Separating the role of zonally asymmetric forcings. *Atmospheric Chemistry and Physics*, *21*(24), (2021). 18499–18518.
24. Allen, R. J., Norris, J. R., & Kovilakam, M., Influence of anthropogenic aerosols and the Pacific Decadal Oscillation on tropical belt width. *Nature Geoscience*, *7*(4), (2014). 270–274.
25. Smith, D. M., Booth, B. B. B., Dunstone, N. J., Eade, R., Hermanson, L., Jones, G. S., Scaife, A. A., Sheen, K. L., & Thompson, V., Role of volcanic and anthropogenic aerosols in the recent global surface warming slowdown. *Nature Climate Change*, *6*(10), (2016). 936–940.
26. Dittus, A. J., Hawkins, E., Robson, J., Smith, D. M., & Wilcox, L. J., Drivers of Recent North Pacific Decadal Variability: The Role of Aerosol Forcing. *Earths Future*, *9*(12), (2021). e2021EF002249.
27. Bonfils, C., & Santer, B. D., Investigating the possibility of a human component in various pacific decadal oscillation indices. *Climate Dynamics*, *37*(7), (2011). 1457–1468.
28. Smith, D. M., Scaife, A. A., Eade, R., Athanasiadis, P., Bellucci, A., Bethke, I., Bilbao, R., Borchert, L. F., Caron, L.-P., Counillon, F., Danabasoglu, G., Delworth, T., Doblas-Reyes, F. J., Dunstone, N. J., Estella-Perez, V., Flavoni, S., Hermanson, L., Keenlyside, N., Kharin, V., … Zhang, L., North Atlantic climate far more predictable than models imply. *Nature*, *583*(7818), (2020). 796–800.
29. Scaife, A. A., Arribas, A., Blockley, E., Brookshaw, A., Clark, R. T., Dunstone, N., Eade, R., Fereday, D., Folland, C. K., Gordon, M., Hermanson, L., Knight, J. R., Lea, D. J., MacLachlan, C., Maidens, A., Martin, M., Peterson, A. K., Smith, D., Vellinga, M., … Williams, A., Skillful long-range prediction of European and North American winters. *Geophysical Research Letters*, *41*(7), (2014). 2514–2519.

30. Scaife, A. A., & Smith, D., A signal-to-noise paradox in climate science. *Npj Climate and Atmospheric Science*, *1*(1), (2018). 1–8.
31. Laguë, M. M., Quetin, G. R., & Boos, W. R., Downwind control of oceanic air by land: The land wake and its sensitivity to CO2. *Environmental Research Letters*, *17*(10), (2022). 104045.
32. Frankignoul, C., Sennéchael, N., Kwon, Y.-O., & Alexander, M. A., Influence of the Meridional Shifts of the Kuroshio and the Oyashio Extensions on the Atmospheric Circulation. *Journal of Climate*, *24*(3), (2011). 762–777.
33. Anderson, B. T., Empirical Evidence Linking the Pacific Decadal Precession to Kuroshio Extension Variability. *Journal of Geophysical Research: Atmospheres*, *124*(23), (2019). 12845–12863.
34. Di Lorenzo, E., Xu, T., Zhao, Y., Newman, M., Capotondi, A., Stevenson, S., Amaya, D. J., Anderson, B. T., Ding, R., Furtado, J. C., Joh, Y., Liguori, G., Lou, J., Miller, A. J., Navarra, G., Schneider, N., Vimont, D. J., Wu, S., & Zhang, H., Modes and Mechanisms of Pacific Decadal-Scale Variability. *Annual Review of Marine Science*, *15*(1), (2023).
35. Kwon, Y.-O., & Deser, C., North Pacific Decadal Variability in the Community Climate System Model Version 2. *Journal of Climate*, *20*(11), (2007). 2416–2433.
36. Smirnov, D., Newman, M., Alexander, M. A., Kwon, Y.-O., & Frankignoul, C., Investigating the Local Atmospheric Response to a Realistic Shift in the Oyashio Sea Surface Temperature Front. *Journal of Climate*, *28*(3), (2015). 1126–1147.
37. Siqueira, L., & Kirtman, B. P., Atlantic near-term climate variability and the role of a resolved Gulf Stream. *Geophysical Research Letters*, *43*(8), (2016). 3964–3972.
38. Dow, W. J., Maycock, A. C., Lofverstrom, M., & Smith, C. J., The Effect of Anthropogenic Aerosols on the Aleutian Low. *Journal of Climate*, *34*(5), (2021). 1725–1741.
39. Kosaka, Y., & Xie, S.-P., Recent global-warming hiatus tied to equatorial Pacific surface cooling. *Nature*, *501*(7467), (2013). 7467.
40. Seager, R., Cane, M., Henderson, N., Lee, D.-E., Abernathey, R., & Zhang, H., Strengthening tropical Pacific zonal sea surface temperature gradient consistent with rising greenhouse gases. *Nature Climate Change*, *9*(7), (2019). 517–522.
41. Maher, N., Wills, R. C. J., DiNezio, P., Klavans, J., Milinski, S., Sanchez, S. C., Stevenson, S., Stuecker, M. F., & Wu, X., The future of the El Niño-Southern Oscillation: Using large ensembles to illuminate time-varying responses and inter-model differences. *Earth System Dynamics Discussions*, (2022). 1–28.
42. Clement, A. C., Seager, R., Cane, M. A., & Zebiak, S. E., An Ocean Dynamical Thermostat. *Journal of Climate*, *9*(9), (1996). 2190–2196.
43. Cane, M. A., Clement, A. C., Kaplan, A., Kushnir, Y., Pozdnyakov, D., Seager, R., Zebiak, S. E., & Murtugudde, R., Twentieth-Century Sea Surface Temperature Trends. *Science*, *275*(5302), (1997). 957–960.
44. Chiang, J. C. H., & Vimont, D. J., Analogous Pacific and Atlantic Meridional Modes of Tropical Atmosphere–Ocean Variability. *Journal of Climate*, *17*(21), (2004). 4143–4158.

45. Zhang, H., Clement, A., & Nezio, P. D., The South Pacific Meridional Mode: A Mechanism for ENSO-like Variability. *Journal of Climate*, *27*(2), (2014). 769–783.
46. Lehner, F., Deser, C., Simpson, I. R., & Terray, L., Attributing the U.S. Southwest's Recent Shift Into Drier Conditions. *Geophysical Research Letters*, *45*(12), (2018). 6251–6261.
47. Mankin J.S., Simpson I., Hoell A., Fu R., Lisonbee J., Sheffield A., Barrie D., NOAA Drought Task Force Report on the 2020–2021 Southwestern U.S. Drought. NOAA Drought Task Force, MAPP, and NIDIS (2021).
48. Scaife, A. A., Camp, J., Comer, R., Davis, P., Dunstone, N., Gordon, M., MacLachlan, C., Martin, N., Nie, Y., Ren, H.-L., Roberts, M., Robinson, W., Smith, D., & Vidale, P. L., Does increased atmospheric resolution improve seasonal climate predictions? *Atmospheric Science Letters*, *20*(8), (2019). e922.
49. Hardiman, S. C., Dunstone, N. J., Scaife, A. A., Smith, D. M., Comer, R., Nie, Y., & Ren, H.-L., Missing eddy feedback may explain weak signal-to-noise ratios in climate predictions. *Npj Climate and Atmospheric Science*, *5*(1), (2022). 1–8.
50. Zhang, W., Kirtman, B., Siqueira, L., Clement, A., & Xia, J., Understanding the signal-to-noise paradox in decadal climate predictability from CMIP5 and an eddying global coupled model. *Climate Dynamics*, *56*(9), (2021). 2895–2913.
51. Kay, J. E., Deser, C., Phillips, A., Mai, A., Hannay, C., Strand, G., Arblaster, J. M., Bates, S. C., Danabasoglu, G., Edwards, J., Holland, M., Kushner, P., Lamarque, J.-F., Lawrence, D., Lindsay, K., Middleton, A., Munoz, E., Neale, R., Oleson, K., … Vertenstein, M. The Community Earth System Model (CESM) Large Ensemble Project: A Community Resource for Studying Climate Change in the Presence of Internal Climate Variability. *Bulletin of the American Meteorological Society*, *96*(8), (2015). 1333–1349.
52. Gillett, N. P., Shiogama, H., Funke, B., Hegerl, G., Knutti, R., Matthes, K., Santer, B. D., Stone, D., & Tebaldi, C., The Detection and Attribution Model Intercomparison Project (DAMIP v1.0) contribution to CMIP6. *Geoscientific Model Development*, *9*(10), (2016). 3685–3697.
53. Huang, B., Thorne, P. W., Banzon, V. F., Boyer, T., Chepurin, G., Lawrimore, J. H., Menne, M. J., Smith, T. M., Vose, R. S., & Zhang, H.-M., Extended Reconstructed Sea Surface Temperature, Version 5 (ERSSTv5): Upgrades, Validations, and Intercomparisons. *Journal of Climate*, *30*(20), (2017). 8179–8205.
54. Rayner, N. A., Parker, D. E., Horton, E. B., Folland, C. K., Alexander, L. V., Rowell, D. P., Kent, E. C., & Kaplan, A., Global analyses of sea surface temperature, sea ice, and night marine air temperature since the late nineteenth century. *Journal of Geophysical Research: Atmospheres*, *108*(D14), (2003).
55. Hirahara, S., Ishii, M., & Fukuda, Y., Centennial-Scale Sea Surface Temperature Analysis and Its Uncertainty. *Journal of Climate*, *27*(1), (2014). 57–75.
56. Schneider, U., Becker, A., Finger, P., Meyer-Christoffer, A., Ziese, M., & Rudolf, B., GPCC's new land surface precipitation climatology based on quality-controlled in situ

data and its role in quantifying the global water cycle. *Theoretical and Applied Climatology*, *115*(1), (2014). 15–40.

57. Mantua, N. J., & Hare, S. R., The Pacific Decadal Oscillation. *Journal of Oceanography*, *58*(1), (2002). 35–44.
58. Trenberth, K. E., & Hurrell, J. W., Decadal atmosphere-ocean variations in the Pacific. *Climate Dynamics*, *9*(6), (1994). 303–319.
59. Zhao, K., Wulder, M. A., Hu, T., Bright, R., Wu, Q., Qin, H., Li, Y., Toman, E., Mallick, B., & Zhang, X., Detecting change-point, trend, and seasonality in satellite time series data to track abrupt changes and nonlinear dynamics: A Bayesian ensemble algorithm. *Remote Sensing of Environment*, *232*, (2019). 111181.
60. Deser, C., Lehner, F., Rodgers, K. B., Ault, T., Delworth, T. L., DiNezio, P. N., Fiore, A., Frankignoul, C., Fyfe, J. C., Horton, D. E., Kay, J. E., Knutti, R., Lovenduski, N. S., Marotzke, J., McKinnon, K. A., Minobe, S., Randerson, J., Screen, J. A., Simpson, I. R., & Ting, M., Insights from Earth system model initial-condition large ensembles and future prospects. *Nature Climate Change*, *10*(4), (2020). 4.
61. Jeffrey, S., Rotstayn, L., Collier, M., Dravitzki, S., Hamalainen, C., Moeseneder, C., Wong, K., & Syktus, J., Australia's CMIP5 submission using the CSIRO Mk3. 6 model. *Aust. Meteor. Oceanogr. J*, *63*, (2013). 1–13.
62. Rodgers, K. B., Lin, J., & Frölicher, T. L., Emergence of multiple ocean ecosystem drivers in a large ensemble suite with an Earth system model. *Biogeosciences*, *12*(11), (2015). 3301–3320.
63. Kirchmeier-Young, M. C., Zwiers, F. W., & Gillett, N. P., Attribution of extreme events in Arctic sea ice extent. *Journal of Climate*, *30*(2), (2017). 553–571.
64. Sun, L., Alexander, M., & Deser, C., Evolution of the global coupled climate response to Arctic sea ice loss during 1990–2090 and its contribution to climate change. *Journal of Climate*, *31*(19), (2018). 7823–7843.
65. Maher, N., Milinski, S., Suarez-Gutierrez, L., Botzet, M., Dobrynin, M., Kornblueh, L., Kröger, J., Takano, Y., Ghosh, R., Hedemann, C., Li, C., Li, H., Manzini, E., Notz, D., Putrasahan, D., Boysen, L., Claussen, M., Ilyina, T., Olonscheck, D., Marotzke, J., The Max Planck Institute Grand Ensemble: Enabling the Exploration of Climate System Variability. *Journal of Advances in Modeling Earth Systems*, *11*(7), (2019). 2050–2069.
66. Rodgers, K. B., Lee, S.-S., Rosenbloom, N., Timmermann, A., Danabasoglu, G., Deser, C., Edwards, J., Kim, J.-E., Simpson, I. R., Stein, K., Stuecker, M. F., Yamaguchi, R., Bódai, T., Chung, E.-S., Huang, L., Kim, W. M., Lamarque, J.-F., Lombardozzi, D. L., Wieder, W. R., & Yeager, S. G., Ubiquity of human-induced changes in climate variability. *Earth System Dynamics*, *12*(4), (2021).1393–1411.
67. Delworth, T. L., Cooke, W. F., Adcroft, A., Bushuk, M., Chen, J.-H., Dunne, K. A., Ginoux, P., Gudgel, R., Hallberg, R. W., Harris, L., Harrison, M. J., Johnson, N., Kapnick, S. B., Lin, S.-J., Lu, F., Malyshev, S., Milly, P. C., Murakami, H., Naik, V., … Zhao, M., SPEAR: The Next Generation GFDL Modeling System for Seasonal to

Multidecadal Prediction and Projection. *Journal of Advances in Modeling Earth Systems*, *12*(3), (2020). e2019MS001895.

68. Bonnet, R., Boucher, O., Deshayes, J., Gastineau, G., Hourdin, F., Mignot, J., Servonnat, J., & Swingedouw, D., Presentation and Evaluation of the IPSL-CM6A-LR Ensemble of Extended Historical Simulations. *Journal of Advances in Modeling Earth Systems*, *13*(9), (2021). e2021MS002565.
69. Tatebe, H., Ogura, T., Nitta, T., Komuro, Y., Ogochi, K., Takemura, T., Sudo, K., Sekiguchi, M., Abe, M., Saito, F., Chikira, M., Watanabe, S., Mori, M., Hirota, N., Kawatani, Y., Mochizuki, T., Yoshimura, K., Takata, K., O'ishi, R., Kimoto, M., Description and basic evaluation of simulated mean state, internal variability, and climate sensitivity in MIROC6. *Geoscientific Model Development*, *12*(7), (2019). 2727–2765.
70. Fyfe, J. C., Kharin, V. V., Santer, B. D., Cole, J. N. S., & Gillett, N. P., Significant impact of forcing uncertainty in a large ensemble of climate model simulations. *Proceedings of the National Academy of Sciences*, *118*(23), (2021). e2016549118.
71. Ziehn, T., Chamberlain, M. A., Law, R. M., Lenton, A., Bodman, R. W., Dix, M., Stevens, L., Wang, Y.-P., Srbinovsky, J., Ziehn, T., Chamberlain, M. A., Law, R. M., Lenton, A., Bodman, R. W., Dix, M., Stevens, L., Wang, Y.-P., & Srbinovsky, J., The Australian Earth System Model: ACCESS-ESM1.5. *Journal of Southern Hemisphere Earth Systems Science*, *70*(1), (2020). 193–214.

Acknowledgments: We're extremely grateful for helpful and thought-provoking comments from John Fasullo, Jennifer Kay, and Isla Simpson.

Funding: Provide complete funding information, including grant numbers, complete funding agency names, and recipient's initials. Each funding source should be listed in a separate paragraph.

Examples:

National Science Foundation grant AGS-2002528 (JK, PD, TS)

NOAA Climate Program Office grant NA20OAR4310400 (AC)

The National Center for Atmospheric Research is sponsored by the National Science Foundation.

Author contributions:

Conceptualization: JK, PD

Methodology: JK, PD

Investigation: JK

Visualization: JK

Funding acquisition: PD, TS

Writing – original draft: JK

Writing – review & editing: JK, PD, AC, CD, TS

Competing interests: Authors declare that they have no competing interests.

Data and materials availability: All model data is publicly available via the Earth System Grid Federation. All observational products are publicly available online via the institution cited herein.

Supplementary Materials

Materials and Methods

Figs. S1 to S6

Tables S1 to S4

References (*51 - 71*)

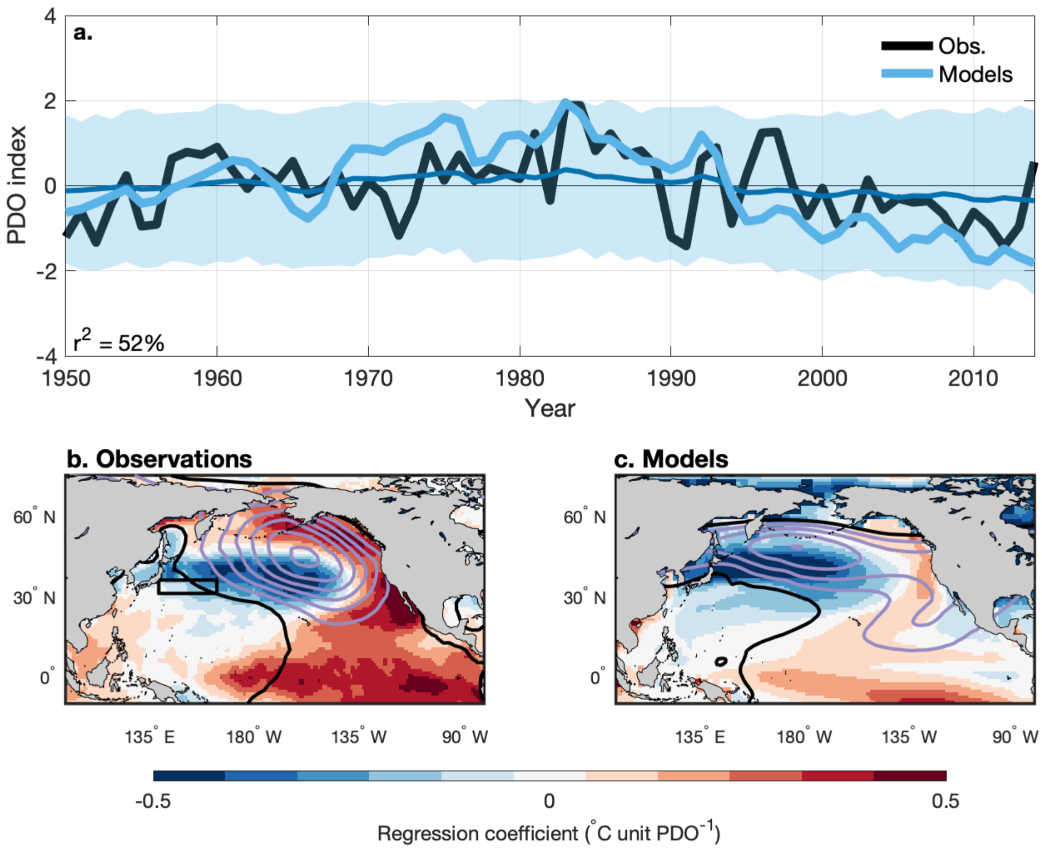

Fig. 1. External forcing explains the timing and pattern of the PDO index. (a) The observed PDO index (black) compared with the ensemble mean PDO index from the all-forcings simulations (dark blue) and the normalized ensemble mean PDO index from the all-forcings simulations (light blue). Note that normalization of the forced PDO scales its amplitude to be equal to observations. The light blue shading encompasses 95% of the PDO indices from individual simulations. (b) Regression of observed SST (colors) and sea-level pressure (contours; hPa per unit of the normalized PDO index). We draw contours every -0.5 hPa in purple; the zero contour is in black.The Kuroshio-Oyashio Extension region is outlined in solid black. (c) as in (b), but the forced components of SST and sea-level pressure have been scaled to have the same standard deviation as observations.

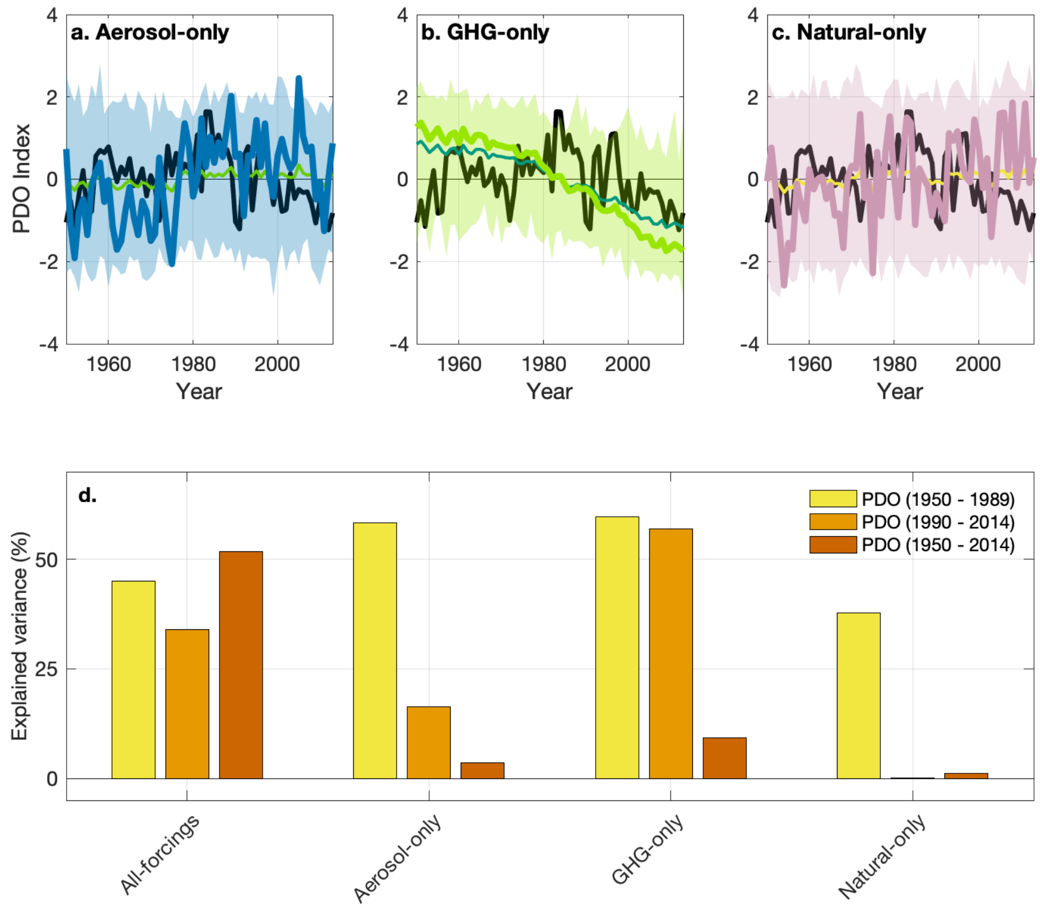

Fig. 2. The interplay of aerosols and greenhouse gases explain the timing of the PDO index. As in (Fig. 1a) but for the ensemble mean of the aerosol-only simulations (a; dark blue), greenhouse gas-only simulations (b; green), and the natural forcing-only simulations (c; purple). The original amplitude PDO index from each single-forcing ensemble is shown in the thin off-colored line. (d) The amount of observed PDO variance explained by the ensemble mean of each of the four suites of simulations for 1950 – 1989, 1990 – 2014, and 1950 – 2014. Note that the correlation between the forced PDO in the GHG-only ensemble and observations between 1950 – 1989 is negative.

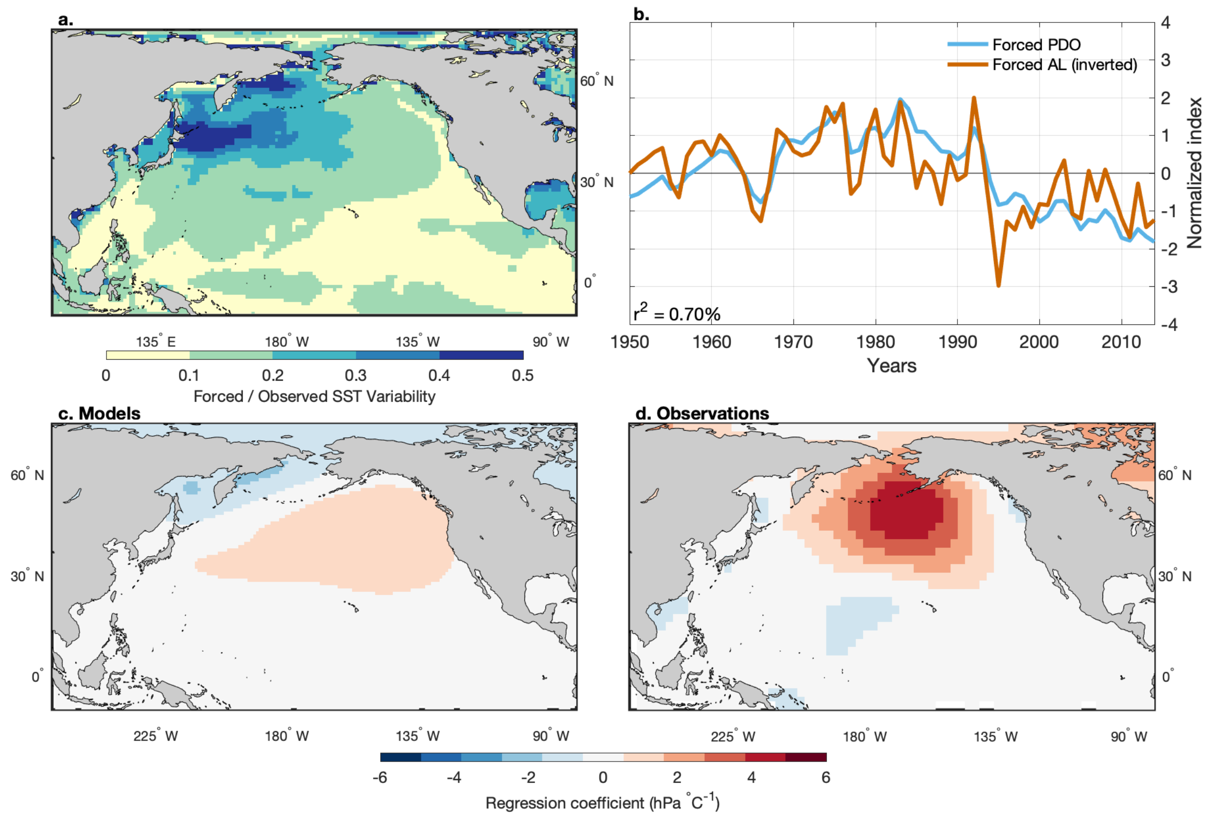

Fig. 3. The signal-to-noise paradox in the PDO is a result of weak Aleutian Low variability. (a) The ratio of forced to total SST variability in models. (b) Timeseries of the forced PDO (from Fig. 1a) along with the strength of the forced Aleutian Low (also known as the North Pacific Index; see Methods) (c) The regression of forced sea-level pressure on an index of forced SST in the Kuroshio-Oyashio Extension region (marked on Fig. 1b) which indicated the strength of the atmospheric response to ocean temperature changes. (d) as in (c) but for observed sea-level pressure and SST.

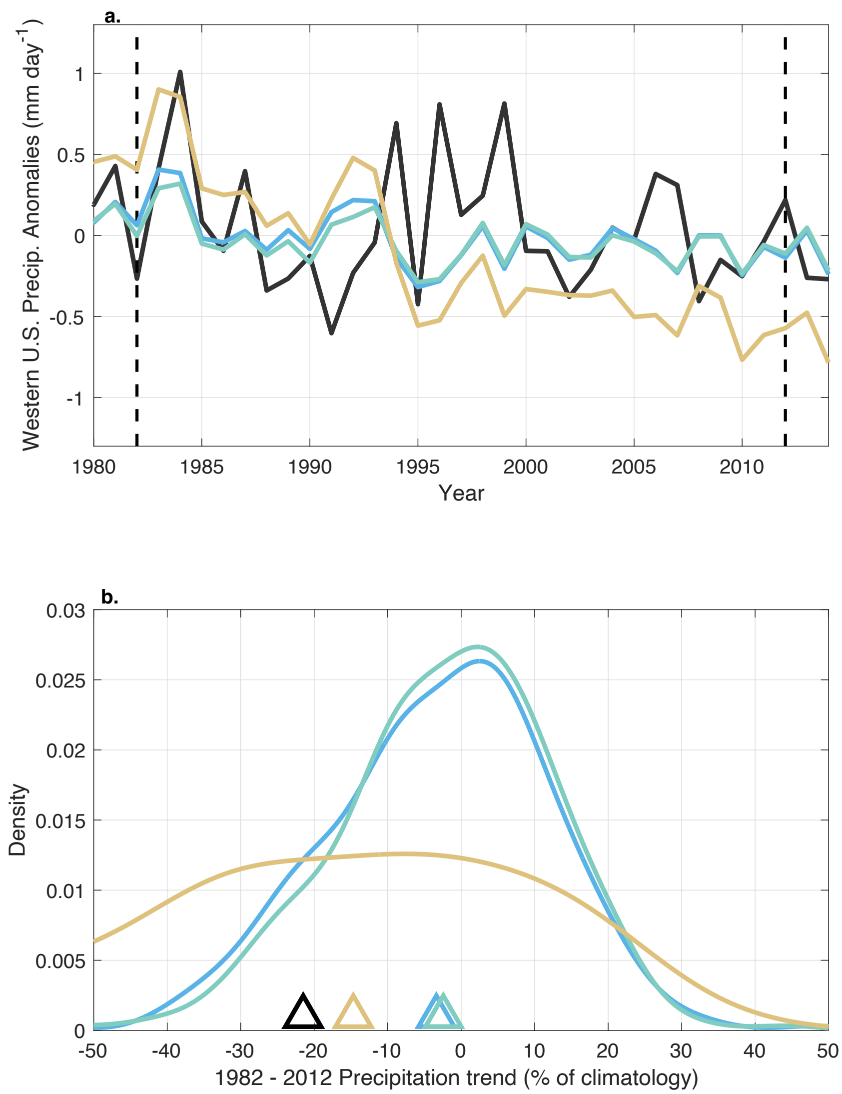

Fig. 4. Long-term drought in the western U.S. is attributable to human emissions of aerosols and greenhouse gases via their influence on the PDO. (a) Timeseries of precipitation in the Southwest U.S. in observations (black), the forced PDO from the all-forcings simulations (blue), the forced PDO from the all-forcings simulations, where the naturally generated PDO in each ensemble has been statistically damped (green), and the forced PDO from the all-forcings simulations, where we substitute a higher amplitude forced PDO for a portion of the naturally generated PDO (see methods). (b) The PDF of the trend in precipitation in the collection of simulations from (a; lines) and their forced components (triangles).

Science
AAAS

Supplementary Materials for

Human Emissions Drive the Pacific Decadal Oscillation

Jeremy M. Klavans, Pedro N. DiNezio, Amy C. Clement, Clara Deser, Timothy M. Shanahan
Corresponding author: jeremy.klavans@colorado.edu

The PDF file includes:

Materials and Methods

Models

We study an extremely large collection of climate model simulations from the last two generations of model development (Table S1). This collection is composed of simulations from 13 individual climate model. We choose models that have at least 20 publicly available simulations each. All simulations are forced with the best estimates of observed external forcing for the full length of each run. The climate trajectory in each simulation is composed of a unique sequence of naturally generated variability not necessarily correlated with the observed variability plus an externally forced response common to all simulations. The forced response includes both anthropogenic global warming and regional climate changes and is isolated by averaging changes in a given climate variable, such as SST, across many simulations (*51*). We consider the time period common to all members, 1950 - 2014. Note that for CMIP5 models, 2006 – 2014 is forced with scenario forcing, not observations. We also consider single-forcing runs from DAMIP (*52*). As mentioned above, each of these runs are forced with one time-varying source of external forcing (industrial aerosols, greenhouse gases, or natural sources).

Observations

We compare the simulations used in this study to the PDO index as calculated by the National Oceanic and Atmospheric Administration (NOAA) National Centers for Environmental Information, using NOAA's Extended Reconstructed Sea Surface Temperature version 5 (*53*). To check for robustness, recalculate the PDO index from the gridded Hadley Centre Sea Ice and Sea Surface Temperature (HadISST) dataset (*54*). This sea surface temperature dataset is also used for the observed temperature maps presented herein. To consider the pattern and strength of the atmospheric circulation over the North Pacific, we use NCEP/NCAR twentieth Century Reanalysis v2c (*55*). For estimates of Southwestern U.S. precipitation, we use a 1° × 1° configuration of the Global Precipitation Climatology Project version 2018 (GPCP) gridded monthly precipitation product covering the years 1901–2016 (*56*).

Indices

In each individual simulation, we calculate the PDO index as the first EOF of North Pacific (20° – 80°N) sea surface temperatures, after subtracting the global mean temperature from each month, at each grid point (*2*). We choose this index because of its historical and ongoing value in forecasting climate impacts (*8, 57*). While different regional rates of anthropogenic warming can alias onto this definition of the PDO (*27*), an alternative definition of the PDO index that only excludes North Pacific spatial average SSTs yields qualitatively similar results for the metrics we put forward in the main text (Fig. S1). To calculate the forced component of the PDO index in models, we average each of these individual PDO indices together. The Kuroshio-Oyashio Extension index is calculated as the area-weighted average SST between 25° – 35°N and 150° – 180°E (*7*). The Gulf of Alaska index is the area-weighted SST between 45° – 60°N and 180°W and 150°E. The North Pacific Index, a measure of Aleutian Low strength is calculated as the area-weighted average sea-level pressure between 35° - 65°N and 160°E – 140°W (*58*). The southwestern US rainfall index is the area-weighted average total precipitation between 31° – 42°N and 125° – 110°W, over land. The forced component any of these indices is calculated as the average across all simulations of the individual indices. The externally forced temperature, pressure, and precipitation fields are calculated as the average of the 4-dimensional fields in each individual simulation. All timeseries are low-pass filtered using a Lanczos filter with a 1/10 year half-power frequency, unless otherwise noted.

Statistical significance

Above, we provide several lines of evidence that there is a significant role for external forcing in the PDO index. We do so to (1) build confidence in our results and (2) to avoid lengthy discourse on the precise accounting for degrees of freedom that would be required for any statistical test. However, in the interest of completeness, we do offer a simple accounting. When comparing the observed and forced PDO timeseries, we have two 65 year-long timeseries ($N = 65$). We low-pass filter these timeseries, thereby reducing the available degrees of freedom. We estimate that there are six available effective degrees of freedom (DoF), following the equation:

$$DoF = \frac{N}{2} * \frac{cutoff}{Nyquist}$$

where the cutoff frequency is 1/10 years and the Nyquist frequency is ½ years. The critical value for a two-tailed test on the Pearson correlation coefficient at the 95% significance level is 0.707. The correlation we estimate between the forced component of the PDO and observations is 0.72, thereby making it significant at the 95% level. There are other methods of calculating the number of effective degrees of freedom that can lead to other interpretations, which is why we rely on other information in this article to assert a role for external forcing.

Precipitation adjustment

We estimate the influence of a more strongly forced PDO in models by replacing part of the naturally-generated PDO with a more robustly forced PDO. In each simulation, we first linearly remove 53% of the total PDO signal from precipitation, at each grid point. We replace this primarily naturally generated signal with the forced PDO-precipitation relationship. That is, we create a counterfactual collection of simulations where the forced PDO has an amplitude that is 53% of observations.

Change point analysis

To evaluate how well the forced component of the PDO simulates observed transitions in the PDO, we use Change Point Analysis. We follow the algorithm in (*59*) as implemented in the Matlab programming language. In observations, this method identifies the highest probability change-point, or a likely change in trend, as occurring in 1998, during the most recent canonical shift in the PDO index. Similarly, this method identifies the highest probability change-point in the forced component of the model-simulated PDO as occurring in 1994. This is excellent correspondence, given the observed PDO has a naturally generated component. We then apply this method to the PDO index from each individual simulation in our collection and record the highest probability change-point. Finally, we construct 90% empirical confidence intervals by yet again applying the same methodology to 582 65-year white noise time series (to match the all-forcings collection), recording the highest probability change point, and calculating the 90% confidence interval of a given year producing a change-point. We plot this in Fig. S1b.

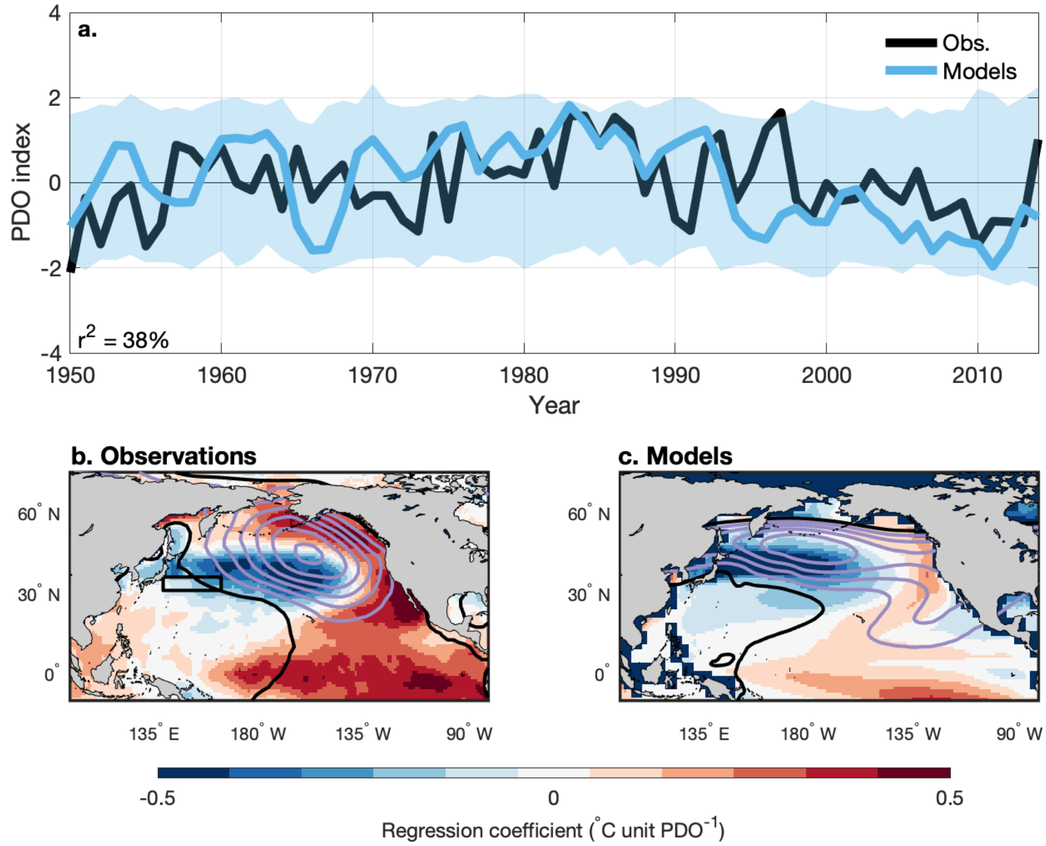

Fig. S1. Sensitivity of the role of forcing to the definition of the PDO index. The PDO index in all panels

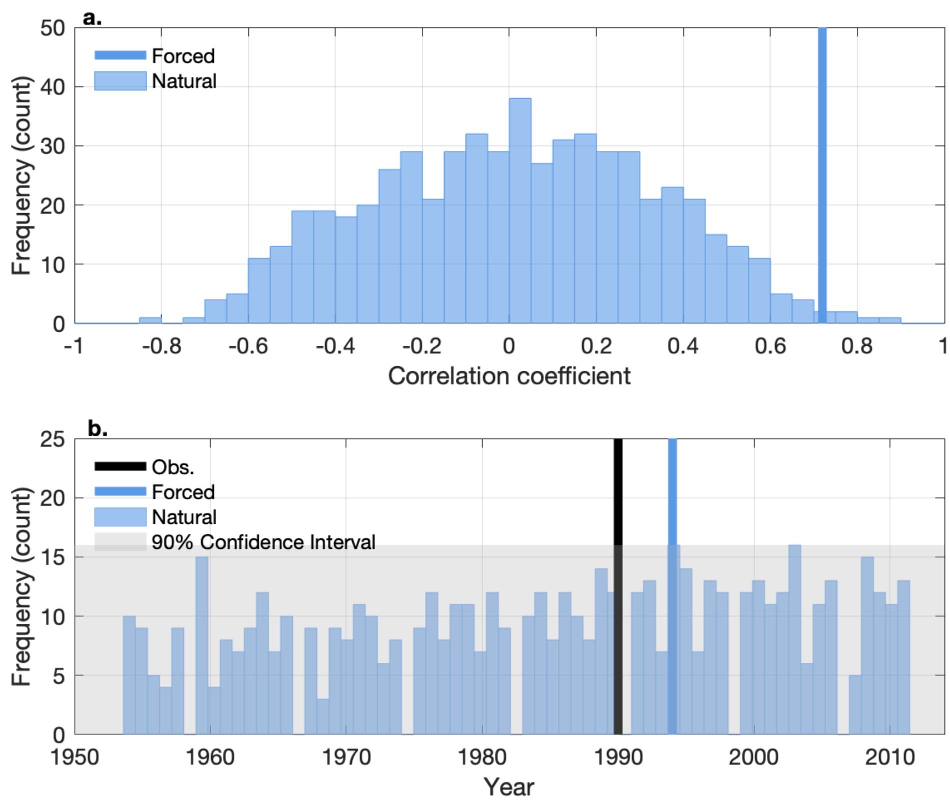

Fig. S2. Comparison of the forced PDO with the natural-only PDO. (a) A histogram of the correlation coefficient between the PDO index in individual simulations, where the forced PDO (from Fig. 1a) has been removed, and observations (bars) as well as the correlation coefficient between the forced PDO and observations (line). (b) Histogram of the estimates of the timing of the most likely change in trend (or "change-point") in individual simulations where the forced PDO has been removed (bars), the most likely change-point in the forced PDO (blue vertical line), and the most likely change-point in observations (black vertical line).

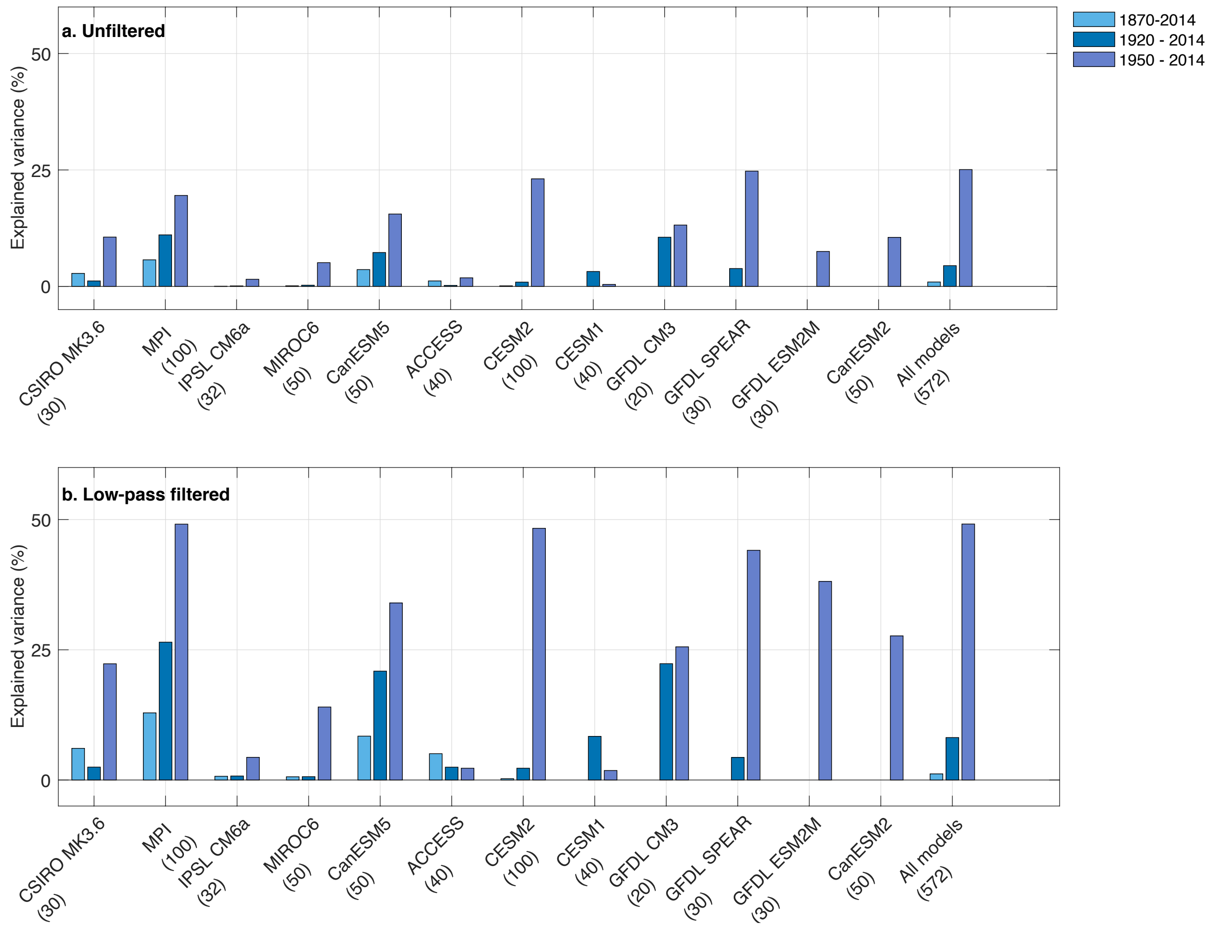

Fig. S3 The evolving role of external forcing in the PDO. External forcing explains more PDO variance after 1950 on both interannual (a) and multidecadal (b) timescales. Please note we only plot bars where model output allows; not all models were initialized prior to 1870 (see Table S1). Also, the number of simulations in each single-model ensemble varies (listed below model name and in Table S1) implying that these bars may not be directly comparable to each other, especially for those models with fewer simulations. Also, the "all models" value varies slightly from the text because we calculate the first principal component of North Pacific SST earlier than 1950 in those models that allow.

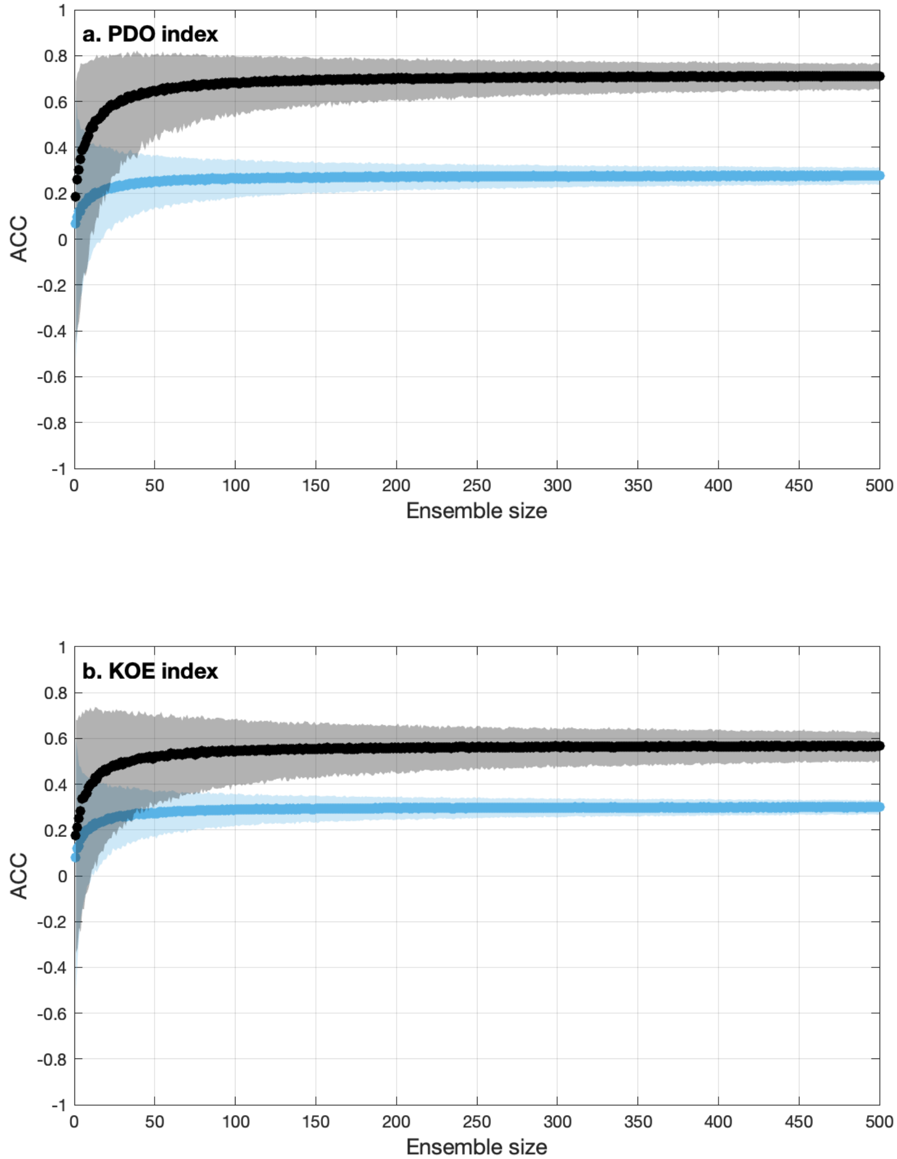

Fig. S4. **The role of ensemble size in extracting the forced component of North Pacific climate variability.** (a) correlation between the observed PDO and the forced component of the PDO (black) as well as the correlation between the forced component of the PDO and a single random ensemble member (blue). (b) as in (a), but for an index of SST in the Kuroshio-Oyashio extension (KOE) region outlined in Figure 1b. The saturation in skill (black line) offers guidance for the size of ensemble needed to isolate the forced component for the PDO. The comparison between the black and blue lines illustrates the signal-to-noise paradox (*29*).

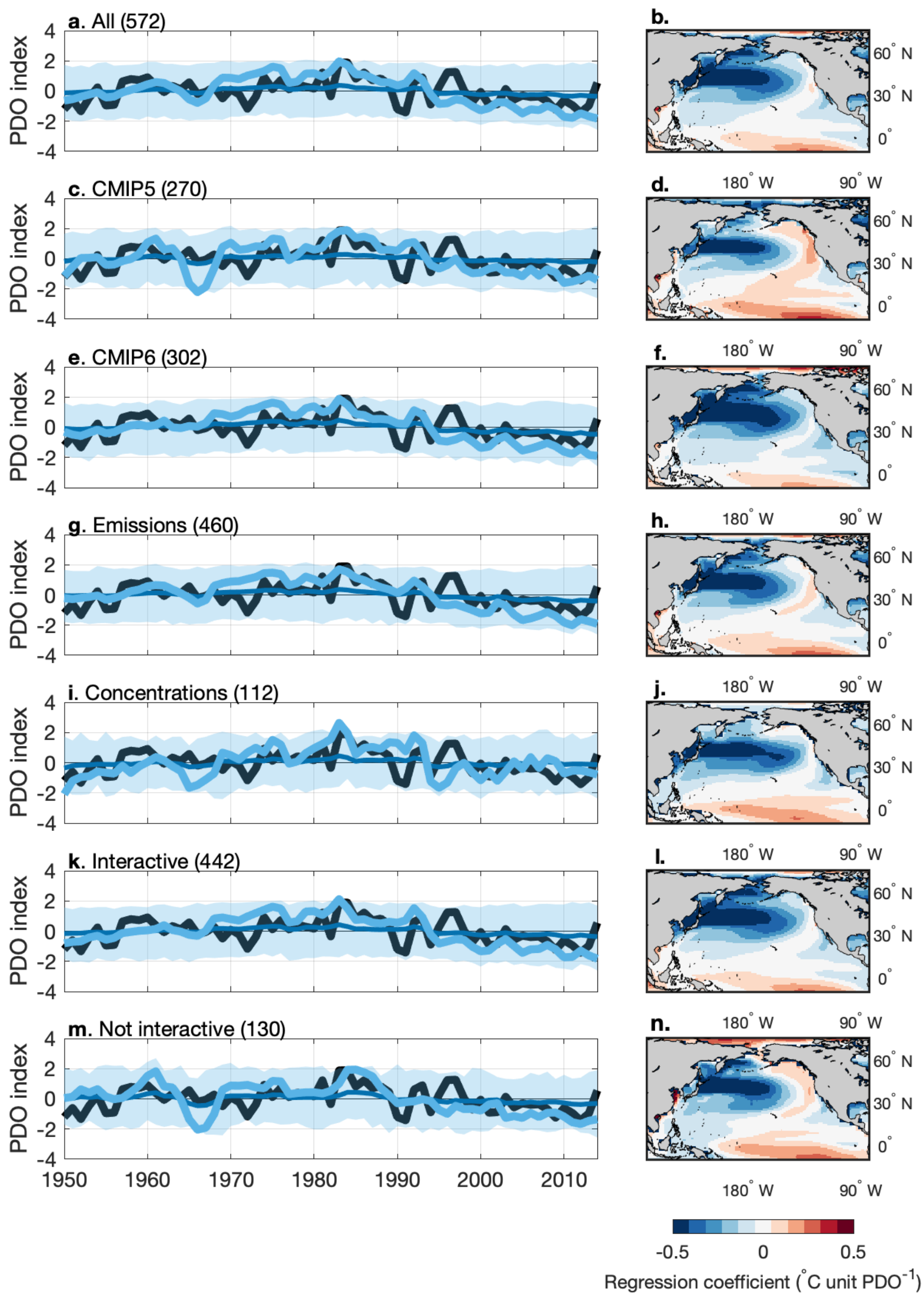

Fig. S5. Testing the sensitivity of the explanatory power of the forced PDO to different model configurations (defined in Table S1). All plots correspond to Fig 1a and 1c. The number of members in each ensemble is listed in parentheses next to the description.

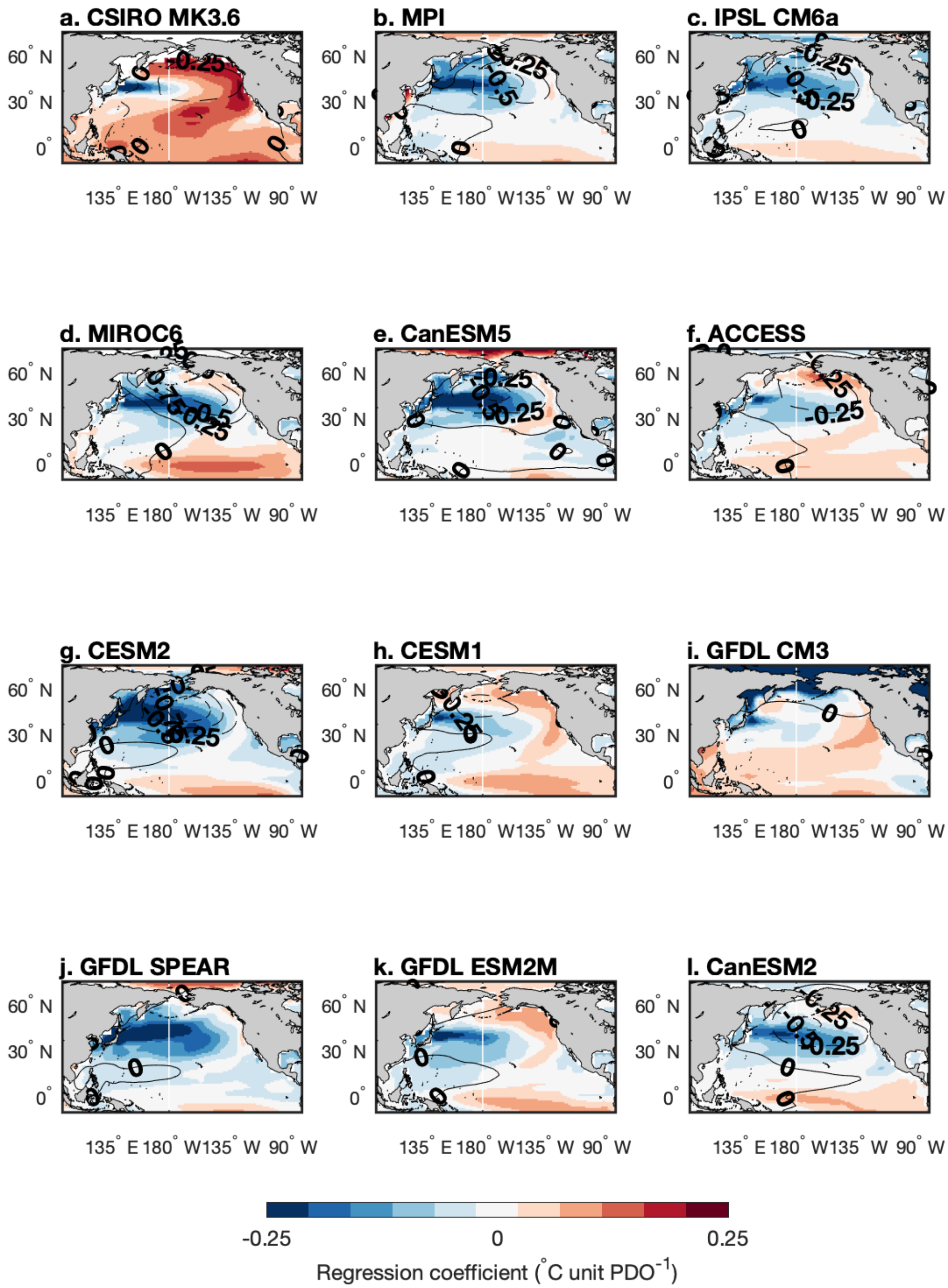

Fig. S6. The forced PDO pattern in each large single-model large ensemble. As in Fig. 1c.

CMIP5 Ensembles	Atmospheric resolution	# of members (270)	Start year	Emissions vs. concentrations	"Fully-interacive" (AR5 Table 9.1)
NCAR-CESM1	1deg	40	1920	Emissions	Yes
GFDL-CM3	2deg	20	1920	Emissions	Yes
GFDL-ESM2M	2deg	30	1950	Concentration	No
CCCma-canESM2	2.8deg	50	1950	Concentration	Yes
CSIRO-Mk3	1.9deg	30	1850	Emissions	Yes
MPI-ESM-LR	1.9deg	100	1850	Emissions	No
CMIP6 Ensembles	Atmospheric resolution	# of members (302)	Start year		Menary et al. (2020)
NCAR-CESM2	1deg	100	1850	Emissions	Yes
GFDL-SPEAR	0.5deg	30	1921	Emissions	Yes
IPSL-CM6A-LR	~2deg	32	1850	Concentration	Yes
MIROC6	~2deg	50	1850	Emissions	Yes
canESM5	~2deg	50	1850	Emissions	Yes
ACCESS-ESM1.5	~1.5deg	40	1850	Emissions	Yes

Table S1: Additional details on the climate models studied (*51, 60 - 71*)

Model	Aerosol-only (75)	GHG-only (82)	Natural-only (129)
canESM5	30	50	50
CNRM-CM6	10	9	10
GISS-E2_1_G	15	10	20
IPSL CM6A LR	10	10	8
MIROC6	10	3	41

Table S2 The single-forcing ensembles and their respective sizes used in this study (from DAMIP; *52*).

Name	**# members**	**r^2 (1950 – 1989) %**	**r^2 (1990 – 2014) %**	**r^2 (1950 – 2014) %**	**S:N PDO**	**S:N KOE SST**	**S:N GoA SST**	**S:N NPI**
All	572	43*	35*	52*	0.19	0.27	0.21	0.09
CMIP5	270	51*	35*	59*	0.15	0.20	0.14	0.09
CMIP6	302	28*	36*	44*	0.25	0.34	0.30	0.11
Emissions	460	37*	44*	50*	0.21	0.28	0.20	0.11
Concentrations	112	57*	3	33*	0.17	0.23	0.28	0.13
Interactive	442	35*	31*	46*	0.20	0.29	0.24	0.09
Not interactive	130	31*	58*	50*	0.22	0.27	0.22	0.12

Table S3 The timing and amplitude of the forced PDO for ensembles of varying model designs (see Table S1). The signal-to-noise ratios estimated in the four right-most columns are calculated as the ratio of forced-to-total variability.

Name	**Total number of members**	**Var. Explained (1950 – 1989) %**	**Var. Explained (1990 – 2014) %**	**Var. Explained (1950 – 2014) %**
Aerosol-only	75	58	16	4
GHG-only	82	60	57	9
Natural only	129	38	0	1

Table S4 Explained variance from single-forcing ensembles described in Table S2. Please note that the correlation coefficient between the GHG-only ensemble mean and observations is negative.